

Supplementary Information for the article

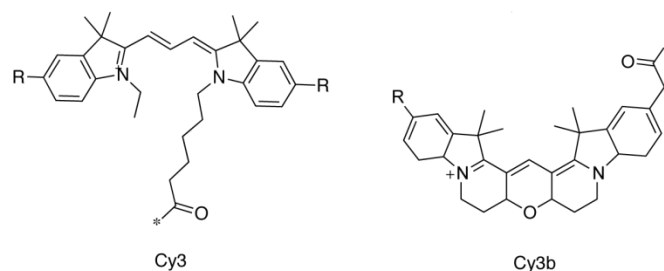
Conformational Distribution of Surface-Adsorbed Fibronectin Molecules Explored by Single Molecule Localization Microscopy

Enrico Klotzsch, Ingmar Schön, Jonas Ries, Alois Renn, Vahid Sandoghdar, Viola Vogel

Materials and Methods

1. Choice of the Cy3B fluorophore

Cy3B is a distant relative of the very common Cy3 cyanine dye. The major difference is that Cy3B is composed of a rigid aromatic system, whereas Cy3 has a conjugated system comprising a central part of alternating single and double bonds along a carbohydrate backbone (see Scheme S1). As a consequence, Cy3 can undergo cis-trans isomerization, whereas Cy3B cannot.



Scheme S1. Structure of cyanine dyes Cy3 (left) and Cy3B (right) used in this study.

This has important consequences:

- The Cy3B dye is brighter and shows a more stable fluorescence emission than Cy3¹. For Cy3, cis-trans isomerization is a major cause of internal de-excitation.
- The Cy3B dye is not expected to show a distinct fluorescence enhancement when interacting with a surface or a protein. It has been shown that the intensity of Cy3 increases in the vicinity of proteins², probably due to a partial immobilization (and therefore avoidance of the cis-trans isomerization). This behavior has been exploited to measure distances based on dye intensity², and the same mechanism is commonly observed for many DNA-binding dyes and was previously exploited by us for the switching of dyes for super-resolution microscopy³.

We rationally chose Cy3B as a fluorophore to optimize the dye performance in stepwise bleaching experiments and to avoid artifacts due to potential interactions at the surface or with Fn itself.

2. Sample preparation

The treated coverslips were clamped/mounted in a custom made aluminum chamber (similar to Invitrogen's "Attofluor Cell Chamber"). 200 μ L of dilute Fn/PBS solution was added to cover the whole accessible surface area of the coverslip. The sample was protected from light during the incubation. After 15 minutes, the solution was exchanged by washing 3 times with 1 mL of PBS. Pipetting was done at the side and slowly to avoid perturbation of the adsorbed proteins. Care was taken to prevent de-wetting of the sample by not completely pipetting out the solution but always leaving enough PBS solution in the chamber that the coverslip was still covered by it. This was especially critical for hydrophobic coverslips where de-wetting can occur quickly. We emphasize that preventing de-wetting is critical for studying Fn conformations under physiological conditions: when de-wetting occurred, we observed larger distances and localizations tended to be aligned along one

direction, probably due to stretched out Fn molecules into the direction along which the de-wetting took place. Finally, the PBS solution was exchanged to 0.5 mL of imaging buffer. The imaging buffer was PBS containing an enzymatic oxygen scavenging system consisting of 0.1 mg/mL glucose oxidase, 0.1 mg/mL catalase, and 2 % (w/v) D+-glucose. All reagents were purchased from Sigma.

3. Microscopy procedure

The principle components of our home-built TIRF setup are described in the main text. The excitation was limited to a round region within the field of view by adjusting the opening of a ring diaphragm which was placed in the beam path before the widefield lens that focused the excitation light onto the back focal plane of the objective. The illumination intensity showed a Gaussian profile and varied by about 40 % over the illuminated region. For taking movies of single molecule bleaching, the following procedure was used: first, the sample was focused by focusing the spots from labeled Fn molecules in one field of view. Second, the laser illumination was blocked by closing an electronic shutter. Third, the stage was moved in one direction by approximately one field of view (~60 μm) using manual x-y translation stages (Thorlabs). This was necessary because molecules in the 'old' field of view have already been bleached during focusing. Fourth, we waited for 45 seconds to minimize the stage drift during image acquisition (see section 10 below). Fifth, the camera acquisition was started. Sixth, the electronic shutter was opened to start the illumination. This procedure was repeated for each movie.

4. Camera settings

The chip of our EM-CCD camera (iXon 897_BV, Andor) was water-cooled to approx. -95 °C. We used the camera in frame transfer mode, the vertical shift time was 3.3 ms, the pre-amplifier gain was set to 1.0x and the EM gain was set to 200. The EM gain of this camera is a 'real' gain and actually gives the average multiplication factor. All movies were recorded with 50 ms exposure time (~20 Hz) for typically 30 sec (600 frames). The camera was controlled using software provided from Andor.

5. Photon conversion

To convert camera counts (=arbitrary digital units: ADU) into the approximate number of photons, we used the following relation:

$$photons = \frac{(counts - offset) * (e^- / ADU)}{EMgain * PreAmpGain} \quad (0.1)$$

Here, a constant offset which is added by the camera to all pixel counts was subtracted. This offset was taken to be 950 and can be measured by the procedure described below. The conversion e^- / ADU was taken as 67.3, as provided in the characterization sheet from the manufacturer. An independent way to measure this conversion factor is described below. In the denominator, the electron-multiplying gain (=200) and the pre-amplifier gain (=1.0) enter.

To measure the offset and the e^- / ADU conversion factor used in equation (1.1), we used an intrinsic property of Poisson noise, namely that the variance in photon counts is proportional to the average (expected) number of photons. A white sheet of paper was placed in front of the dry objective and illuminated by a dim white LED. Images were acquired using the same camera settings as in the stepwise bleaching experiments, but with different exposure times of 5, 10, 15, ..., 100 ms. Care was taken to stay within the linear regime of the dynamic range of the camera, i.e. to avoid oversaturation. A homogeneously bright region was selected in the images and the variance and mean value of all pixels within this ROI was calculated for each image. A plot of the variance versus the mean intensity of was fitted by a first order polynomial using a least square fit. The value where the fit intersects with the x-axis is the offset that is added by the camera to all pixels. The slope is equivalent to the conversion factor including EM gain and PreAmpGain, thus needs to be multiplied by these two gains to obtain the 'bare' e^- / ADU factor. The average value from measurements with

different EM gains was 66.1 for the conversion factor, in good agreement with the value provided by the manufacturer. The offset resulted as 950, as also has been observed by others using the same camera model but a different calibration procedure (see Fig. S6 in the Supplement of reference ⁴).

It should be noted that the back-conversion of counts (electrons) into photons is strictly speaking not possible, because the electron-multiplication step is stochastic in its nature and thus always produces a distribution of counts even for a constant number of photons (see Supplement of Ref 4). As a consequence, the time traces should only be seen as approximations to the actual number of photons. Moreover, also the localization analysis would need to include this additional distribution for Maximum Likelihood estimation (MLE). This can be done (see Ref 5) but is computationally very demanding. On the other hand, the analysis using the simpler photon-count conversion and MLE for ideal Poisson-distributed data has been shown to reach the Cràmer-Rao lower bound in practical applications ⁶. We thus stick to the latter approach because it is simpler but yet powerful.

6. Selection of spots

Movies were imported into a custom-written program in LabView v2010 (National Instruments) with NI Vision. The analysis software can be obtained upon request from one of the authors (I.S.).

Camera counts were converted into photon counts as described above. Movies were cropped in order to remove the dark frames in the beginning (before the start of the illumination); also the first (partially) illuminated frame was discarded. Local maxima were detected by averaging the first 5 images of the cropped movie, high-pass filtering to remove uneven background, smoothing (low-pass filtering) by a 3x3 median filter for two sequential times, intensity-thresholding at a user-defined threshold (interactively), and then choosing those pixels whose 8-connected neighborhood all had smaller values. Local maxima were automatically discarded when they were less than 6 pixels away from the image boundary or at a distance closer than 9 pixels from the next local maxima (to exclude overlapping spots). ROIs of 13x13 pixels centered at the remaining local maxima were further analyzed. Intensity time traces were constructed by summing up all pixel values within the ROI for each frame of the cropped movie.

7. Step finding routine

The detection of steps was automated, but selection of bleaching traces for further analysis was done interactively. For the automatic detection of steps, we adapted a step-finding routine that is in detail described in the Supplement of reference ⁷. Briefly, the routine creates a list of best least squared error fits with $n=1,2,\dots,10$ steps under the boundary condition that the distance between steps is at least 4 frames. The requirement of a minimum plateau width of 4 frames was chosen to exclude the fitting of single 'outliers' (extreme variances in noise). The 'best' step position within a window is determined by creating least square fits for all possible positions and selecting the one having the largest 'area' underneath the new plateau, determined by the step height multiplied by the square root of the plateau length. For selecting the 'most probable' number of steps, we used a phenomenological rule based on the combination of different criteria. One criterion was the so called 'quality ratio' (QR) as introduced in the original routine ⁷ which is derived from a 'counter fit' with the same number of steps placed in-between the 'best' step positions. A second criterion was the relative change in the 'area' (relA) under the best trace with n steps compared to the best trace with $n-1$ steps, normalized to the $n-1$ step area: $relA = (A_n - A_{n-1}) / A_{n-1}$. The third was the residual sum of squares (RSS). These three were combined into a single measure according equation (1.2):

$$criterion = QR * relA / RSS \quad (0.2)$$

The position of the peak of this criterion was chosen as the 'most probable' number of steps. Compared to the original QR, our criterion tends to pick as less number of steps as possible to approximate the time trace. It does allow for downward as well as upward steps, and thus also fits traces that show moderate blinking of dyes. To exclude traces with mis-positioned steps or blinking, we manually selected the spots that showed a 'clean' bleaching behavior.

It should be noted that the requirement of a minimum plateau width of 4 frames leads to a bias in the selection (number) of traces that show different number of bleaching steps. A bleaching trace with 4 steps is more likely to contain two steps which come closer than four frames than is a bleaching trace with only 2 steps. This is why the distribution of the number of Fn molecules that bleached in 4, 3, or 2 steps (see Fig. 2) was not well described by a binomial distribution that is expected. When one assumes equal probabilities for the 4 labeling sites, the distribution should be binomial. The probability for each site can be inferred from the average number of labels per molecule which was 3.7 (as determined from absorption measurements), and results as 92.5 %. It thus would be expected to see more 4 step bleachers than 3 step bleachers than 2 step bleachers. The observed distribution based on our selection criteria does not follow this expectation, but the discrepancy is consistent with the above argument that traces with many steps are underrepresented.

8. Variation in step heights

The observed bleaching time traces showed some variation in step heights (see Fig. 1). Differences from spot to spot are mainly due to the inhomogeneous illumination intensity over the field of view (see section 3 above). However, steps within single bleaching traces should have equal height under ideal conditions. Deviations can have two origins: dyes can have different brightness, or two (or more) steps coincide and are observed as a single step. In the latter case, the expected step is about two-(or more)-fold higher compared to other steps. We typically did not include such spots in the latter analysis. The observed variations in step height of up to ~30% within single traces are well below this expectation and render this explanation unlikely. We thus think that the fluorophores differed in their brightness which can – in general – have several reasons:

- i) The local chemical milieu can affect the proportion of time that the dye resides in a dark state. E.g. the accessibility of the dye to molecular oxygen which is a potent triplet state quencher (not to be confused with oxygen radicals which lead to dye bleaching) as well as to reducing or oxidizing reagents which can either bring the dye from its triplet state into a dark state or recover it from a dark state to its ground state¹ can dramatically affect dye brightness and longevity. In our case, Cy3B was conjugated to cysteines that are buried within Fn type III modules 7 and 15. For labeling these sites, Fn was chemically denatured and then refolded. It is not known how shielded the dyes are at these position, i.e. if they are buried inside the modules or (partially) stick out of the modules. It is very well possible that the accessibility of dyes varies from module to module. This would be a possible explanation for the observed differences in step height.
- ii) Attractive interactions of the dye with surfaces in its vicinity can lead to a (partial) immobilization of the dye. In general, this could have two major effects: on one hand, the cis-trans isomerization of the dye could be restricted, leading to a fluorescence enhancement. As pointed out in section 1 above, Cy3B cannot undergo cis-trans isomerization, thus the effect of the environment on the conjugated system of the dye should be small. On the other hand, an immobilization hinders the rotational movement of the dye. As a consequence, the dipole moment of the dye adopts a fixed orientation which affects both its excitation as well as its emission efficiency, depending on the polarization of the illumination. A fully fixed orientation leads to distinct ‘dipole patterns’ of its point spread function (PSF): the shape varies between elliptical over round to even doughnut-shaped spots, depending on the angle between the dipole moment and the surface normal (see e.g. Supplement of Ref. 3). Fitting these patterns with a symmetric Gaussian PSF model can lead to systematic errors in the localization of up to 10 nm³. In our experiments with labeled Fn, we did not observe deviations from the approximately Gaussian spot shape that is expected for rotationally averaged dipole orientations. We did very well observe such patterns when imaging Cy5 dyes bound to DNA origami structures on coverslips using the same method (unpublished data). We thus conclude that dye immobilization did not play a major role for the Cy3B-labeled Fn molecules.

However, we do not exclude partial immobilization on time scales shorter than the exposure time (50 ms), which could affect the brightness of the dye from frame to frame but should not affect its average brightness.

We would like to note that a different brightness of the dyes itself does not dis-evaluate or negatively affect their localization by the stepwise bleaching analysis, as long as each dye has a constant brightness. The brightness of course limits the achievable precision of its localization, but it does not lead to any systematic errors. The localization technique is therefore much less affected than intensity-based methods such as FRET.

9. Dye localization

The localization of single fluorescent emitters was done as follows: for each selected ROI and for each step, four images before and after the step were summed up and the sum image after the step was subtracted from the sum image before the step. A constant offset was added to this difference image to ensure positivity and to approximate the homogenous photonic background in the original image. This offset was determined from the minimum pixel value of the sum image before the step. Each difference image was then fitted using a symmetric pixelated Gaussian PSF model using a Maximum Likelihood estimator for Poisson distributed data⁶. The fitting was done using LabView's in-built non-linear Levenberg-Marquardt routine that was modified to allow for Maximum Likelihood estimation according to published procedures⁸. For fits that showed a variation of more than 30% in brightness between dyes, as well as PSF widths (sigma of Gaussian) larger than 150 nm the corresponding patterns were excluded from further analysis to eliminate patterns where one or more dye could have potentially had a fixed dipole orientation which typically leads to intensity variations and changes in PSF shape. The performance of the fitting routine was verified using Monte Carlo simulated data; this test showed that the fitting routine reached the Cràmer-Rao lower bound (CRLB)⁶.

The limitation of the localization analysis to 4 frames before and after each step was motivated by the following considerations:

- i. The subsequent analysis of distance distributions assumes that each distance has the same measurement precision. Taking a constant number of frames limits the variation in the number of photons obtained from different dyes, which enters their localization precision and therefore also the error of the inter-label distances⁹. If the distances had different associated errors, these still could be accounted for in the calculation of a mean value by using them as weights, but they cannot be handled appropriately when using quartiles (i.e. the median) to characterize an unknown (non-normal) distribution.
- ii. Stage drift during the measurement (see section 10 below) has consequences for the fitting procedure. When the stage was moving during a plateau in the bleaching trace and images are summed up, the PSF of one dye is not symmetric anymore but becomes elongated in the direction of movement. Therefore it is not justified to use a symmetric PSF for fitting. For the dye(s) that are present before and after the bleaching step, their summed images from before the step and after the step are displaced by the stage drift. Subtraction thus will leave behind not only noise but also a systematic pattern with an increased fluorescence on one side (opposed to the direction of stage movement) and a decreased fluorescence on the other side (in the direction of stage movement). This residual fluorescence pattern systematically distorts the to-be-fitted PSF and can lead to systematic displacements of the fitted location (opposed to the direction of stage movement). Both effects can be minimized by only using frames that are close to the step, which also limits the effective drift during this time window.

We would like to note that the optimum localization precision can be achieved only when using all available information (all frames), thus not limiting the analysis to windows around the steps. To this end, the stage drift needs to be determined independently and be used to correct for the x-y parameters in the model PSFs for each frame, while all frames containing different number of model PSFs must be fitted in parallel. This procedure is doable but computationally demanding. As the stage drift in our setup was shown to be tolerable (it worsened the measurement precision by <3 nm), we did not try to establish this rigorous fitting procedure and did not use fiducial markers to determine the stage drift for each measurement. Using the full information also demands for advancements of the analysis of distance distributions that can deal with different measurement precision for individual distance measurements.

10. Stage drift

To quantify the stage drift in the x-y plane over time, a coverslip was mounted in our sample holder, coated with poly-L-lysine by adsorption from solution (1mg/mL in PBS for 30 min), and incubated with fluorescent beads (YG beads, 0.2 μm diameter, PolySciences Inc.). After washing, the immobilized beads were imaged in PBS on our TIRF setup. For determining the stage drift, we started the image acquisition right after having translated the stage by one field of view. The bead movement was then analyzed by fitting the position of individual beads in each frame, linking the x-y-positions of one bead for subsequent frames, and averaging all x-drift traces and y-drift traces of all analyzed beads within one movie, respectively. The x- and y-position showed an initial drift with a rate of up to 5 nm/sec which typically ceased after \sim 10-15 seconds. After this initial mechanical equilibration, the drift was less than 600 nm/h (10 nm/min). We thus introduced a waiting time of \sim 45 sec before starting a measurement (see section 3 above) to minimize the drift during the measurements. As typical times for bleaching traces were on the order of 10-15 sec (see Fig. 1), the stage drift was limited to about <3 nm. As we pointed out in the preceding section, we thus did not correct the localization analysis for this drift. We also would like to emphasize that the experimentally determined measurement precision using the DNA ruler (see Supplementary Fig. S1) already include the error arising from stage drift, which proves that drift did not significantly impair our measurement precision.

11. Calibration of pixel size

The actual pixel size was determined by imaging a normalization grating (metal grid for electron microscopy; mesh size 12.7 μm) and then measuring the distances between edges several times. The average from these measurements resulted in a pixel size of 92 nm.

To test the pixel size calibration, we immobilized 100 nm fluorescent beads to a coverslip. A piezoelectric stage (Tritor T-403-21D, Piezosystems Jena) was used to translate the sample in defined steps of 35 nm. At each position, 10 frames with 50 ms exposure time each were recorded. For each image the bead was localized by fitting its PSF to a two dimensional Gauss-distribution. The position in the direction of translation was plotted versus frame number and a step finding routine⁷ was used to detect steps (Figure S1 A). The histogram of step sizes had a mean value of 35.9 ± 2.9 nm (Figure S1 B). The relative error compared to the expected step size of 35 nm thus was 2.6%. We conclude that the calibration of the pixel size was accurate up to 2.6 %.

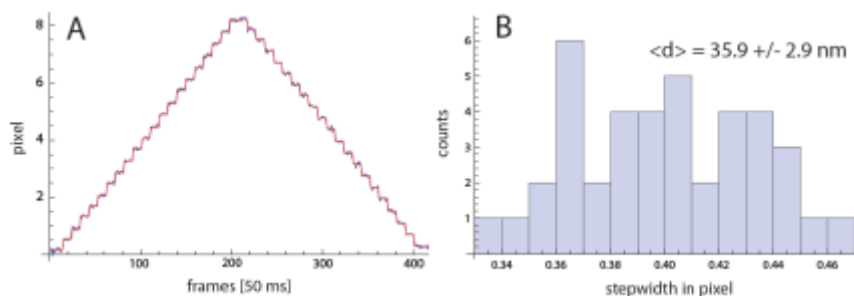


Figure S1. Stepping of fluorescent beads. The sample was displaced laterally by a piezoelectric stage with controlled stepsizes of 35 nm. (A) Displacement of a bead over time. Shown are fitted bead positions (blue) and the best fit of this time trace with a step-finding routine (red). (B) Histograms of the fitted step heights obtained from the step-finding routine. The average of 35.9 nm is in good agreement with the step size of the piezoelectric stage.

12. Control measurements using a DNA ruler

To verify the accuracy of our distance measurements with the stepwise bleaching method, 40 base oligos labeled at their 5' and 3' ends with Cy3 (5'-Cy3-ATA GTG GAA TCG CAA TGT AGC CTC GTC TGG ATG TCT A-Cy3-3', Metabion) were annealed with unlabeled complementary strands and used as a 40*0.33nm=13.2 nm calibration ladder. Polylysine-coated 8-well chambers (NUNC) were incubated with 5 nM DNA in PBS for 5 min and then washed twice to remove unbound DNA. Movies were recorded and 2-step bleachers were analyzed as described above. The obtained distance distribution was fitted by the theoretically expected distribution⁹ using MLE. The fit yielded a mean of 10.9 nm and a precision for this distance of 3.7 nm (Figure S2).

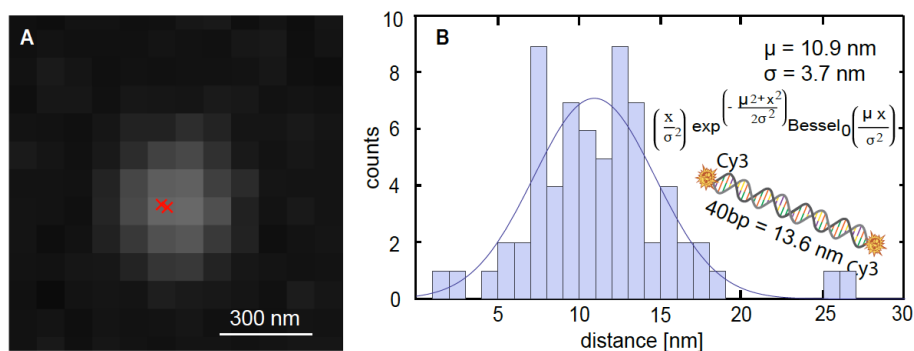


Figure S2. Distance measurements using a DNA ruler of a nominal length of 13.2 nm. Data (histogram) were well fitted by a distance distribution using the relation from reference⁹.

The reasonable agreement between the found distance ~ 11 nm and the expected distance ~ 13 nm validates our measurements/analysis. The precision of 3.7 nm for the distance implicates a localization precision for the individual dyes of 2.6 nm (see reference⁹). This precision is higher than that expected for the Cy3B dye estimated based on the number of collected photons for the Fn measurements (see section 2.3 in the main text). This difference was due to a higher illumination intensity that we used for the DNA experiments; the illumination intensity was reduced for the Fn experiments because more steps needed to be resolved and therefore photobleaching needed to be slowed down.

13. Modeling surface-adsorbed, denatured Fn as a 2D worm-like chain

For estimating the expected distance distribution of labeled Fn adsorbed to a glass surface under denaturing conditions, we propose a model based on the following assumptions/findings:

- Denatured proteins behave as an unstructured and flexible polypeptide chain.
- It has been shown that unstructured loops in proteins¹⁰ as well as proteins that undergo mechanical unfolding¹¹ can be modelled as worm-like chains (WLC) with a persistence length of 0.3-0.4 nm.

- iii. We assume that the denatured polypeptide chain adopts a flattened configuration upon adsorption, and thus the conformational freedom of the polymer is effectively restricted to a d=2 embedding space (2 dimensions rather 3).
- iv. The formula for the end-to-end distance of a WLC can also be applied to the distance between two internal chain modules when using the number of segments in-between these modules for the end-to-end WLC formula.

A WLC is characterized by its contour length $l_c = N \cdot l_0$ (resulting from N segments of finite length l_0 each), and by its persistence length l_p . The distribution function $p(\xi, r)$ of the end-to-end distance R is usually derived in rescaled coordinates normalized to the contour length, viz. radius $r \equiv R/l_c$ and persistence length $\xi \equiv l_p/l_c$. The end-to-end distance distribution of a 2-dimensional WLC in the Daniels approximation for floppy $\xi < 0.1$ polymers is approximately given by (see equation 3.2 in reference¹²):

$$P_{2D}(\xi, r) = \frac{2\pi r}{\Theta} \cdot p(\xi, r) = \frac{2\pi r}{\Theta} \cdot e^{-r^2/\xi} \cdot \left[\frac{1}{\xi} \left(1 + \frac{5}{4} r^2 \right) - \frac{7}{32\xi^2} r^4 - \frac{3}{4} \right] \quad (0.3)$$

Here, Θ is a normalization constant that ensures that the integral from $r=0$... 1 equals 1 and was computed to take the form:

$$\Theta = \frac{\pi}{32\xi} \left[e^{-1/\xi} (2\xi(\xi + 29) - 7) - 2\xi(\xi + 16) \right] \quad (0.4)$$

The end-to-end distribution $P_{2D}^*(R, N)$ for the non-normalized WLC are obtained by a simple back-substitution and normalization by the contour length:

$$P_{2D}^*(R, N) = \frac{1}{Nl_0} P_{2D}(l_p/Nl_0, R/Nl_0) \quad (0.5)$$

For modeling Fn as WLC, we used a segment length of $l_0 = 0.38$ nm for the distance between C^α atoms in the polypeptide backbone. The number of segments N was obtained from fibronectin's primary sequence (P02751, www.uniprot.org). The labeling sites in the type III modules 7 and 15 are separated in the primary sequence by 750 amino acids. The number of amino acids between modules type III 15 on the dimer arms is 840 amino acids. Other possible distances thus result as $750+840=1590$ amino acids between FnIII7 and FnIII15 on different arms, and $2*750+840=2340$ amino acids between FnIII7 and FnIII7 on different arms (see Supplementary Figure S3 A).

For monomeric Fn, the distance distribution between labeling sites was described by

$$P_{monomericFn}^* = P_{2D}^*(R, 750) \quad (0.5)$$

For dimeric Fn, the distance distribution between labeling sites was taken as statistical combination of all inter-label distances:

$$P_{dimericFn}^* = 1/6 \cdot \left[2P_{2D}^*(R, 750) + P_{2D}^*(R, 840) + 2P_{2D}^*(R, 1590) + P_{2D}^*(R, 2340) \right] \quad (0.5)$$

These distributions were fitted to the distance data of reduced Fn at 4 M GdnHCl and native Fn at 4 M GdnHCl, respectively, using maximum likelihood estimation and the persistence length as free parameter. The data were fitted well by the WLC distributions of equations (1.6) and (1.7) yielding persistence lengths of 7.4 ± 0.7 nm for monomeric Fn and 8.5 ± 1.0 nm for dimeric Fn, respectively (see red lines in Supplementary Figure S3 B+C).

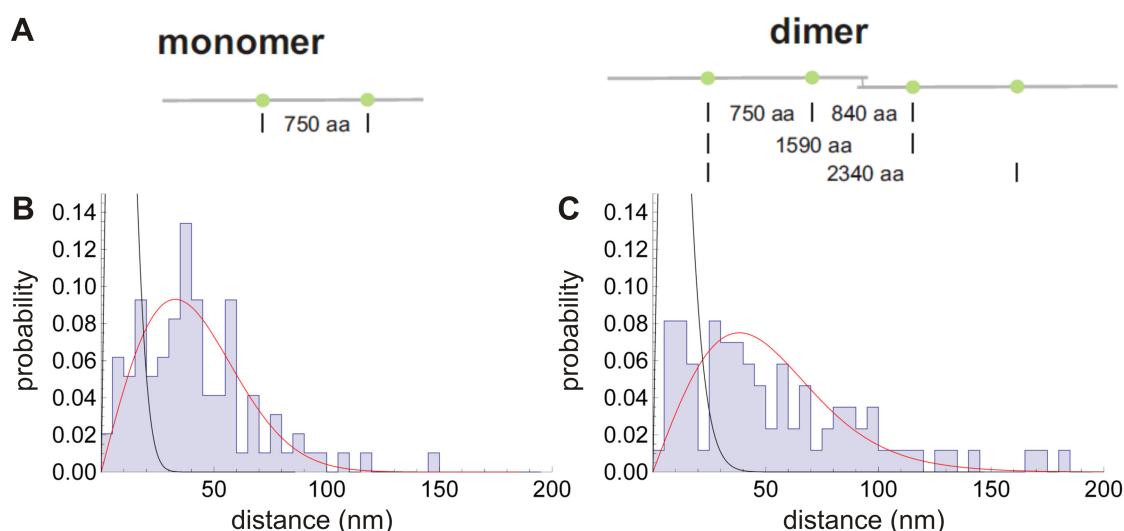


Figure S3. Worm-like chain model of denatured adsorbed Fn. A) Schematic of intra-label distances according to the primary sequence of Fn. B)+C) Distance histogram for monomeric (B) or dimeric (C) Fn at 4M GdnHCl. Red lines: fit by WLC model resulting in a persistence length of 7.4 ± 0.7 nm (B) or 8.5 ± 1.0 nm (C). Black lines: WLC model assuming a 'free' persistence length of 0.4 nm.

The two fitted persistence lengths are consistent with each other. This agreement to some extent justifies the assumption that the Fn sequences between labels can be modeled as independent WLCs.

The value of the fitted persistence length (~ 8 nm) is about 20 times higher than the persistence length $l_p = 0.4$ nm of a flexible polypeptide chain in 3D¹⁰. This result was unexpected: the assumptions that underlie the 2D WLC model predict the same persistence length for the 2D and the 3D situation, as the only difference in the models are the dimensions. Using a persistence length of 0.4 nm resulted in distance distributions that severely underestimated the observed distributions for monomeric as well as dimeric Fn (see black lines in Supplementary Figure S3 B+C).

Two scenarios might explain this discrepancy: on one hand, in the experimental situation the Fn polypeptide chain interacts with the surface by attractive interactions of different origins (electrostatic, van-der-Waals, hydrophobic). These interactions are not part of the WLC model. We imagine that Fn-surface interactions effectively restrict chain-internal degrees of freedom which could lead to an increased 'effective' persistence length. Conceptionally, this is equivalent to lowering the temperature of the system which has been shown to correlate with larger dimensions of denatured proteins¹³. On the other hand, it is likely that excluded volume effects (surface adsorption 'sites' that are already occupied by other parts of the chain) are severely underestimated by the model, i.e. for floppy chains like in the case of a long polypeptide where the rescaled persistence length was expected to be $\zeta < 0.0014$. Excluded volume effects thus might lead to a distinct increase of end-to-end distances of polypeptides interacting with (and restricted to) a surface.

In conclusion, we think that not all of the assumptions that underlie the WLC model are valid. Thus, a simple WLC model based on the persistence length for flexible polypeptides does not accurately describe conformations of denatured Fn at surfaces. Further research is needed to clarify whether the behavior of flexible polypeptides that interact with a surface can be described by a 2D WLC with an 'effective' persistence length that depends on the strength of these interactions, as it is implied by our results here.

It should be noted that the observed distance distributions are a result of a convolution of the true distance distributions with the distribution due to the limited measurement precision⁹. For the 2D

situation, the non-Gaussian distance distribution for a single distance μ with precision σ is given by (equation 4 in reference⁹)

$$p_{\text{measurement}}(R, \mu) = \frac{R}{\sigma^2} \exp\left(-\frac{\mu^2 + R^2}{2\sigma^2}\right) I_0\left(\frac{R\mu}{\sigma^2}\right) \quad (0.5)$$

Here, I_0 is the modified Bessel function of zero order. As a consequence, the probability distributions for monomeric and dimeric Fn (equations (1.6) and (1.7) above) need to be convolved by the distribution arising from the limited measurement precision

$$P_{Fn}^{**}(R) = \int_0^\infty P_{Fn}^*(\mu) \cdot p_{\text{measurement}}(R, \mu) d\mu \quad (0.5)$$

These distributions then must be fitted to the observed data. In general, the fitted persistence lengths are smaller because the convolution broadens the true distributions and shifts them to larger distances. For example, assuming a precision of ~ 7 nm for distance measurements, the best agreement between fit and data is obtained for persistence lengths of about 7 nm (monomeric Fn) and 8 nm (dimeric Fn). These numbers are not significantly smaller than the ones obtained by the direct fitting, indicating that the measurement precision that we had in experiments did not significantly impact the interpretation of measured distance histograms.

References

1. J. Vogelsang, R. Kasper, C. Steinhauer, B. Person, M. Heilemann, M. Sauer, and P. Tinnefeld, *Angew. Chem. Int. Ed.*, 2008, **47**, 5465–5469.
2. H. Hwang, H. Kim, and S. Myong, *Proc Natl Acad Sci U S A*, 2011, **108**, 7414–7418.
3. I. Schoen, J. Ries, E. Klotzsch, H. Ewers, and V. Vogel, *Nano Lett.*, 2011, **11**, 4008–4011.
4. M. H. Ulbrich and E. Y. Isacoff, *Nature Methods*, 2007, **4**, 319–321.
5. K. I. Mortensen, L. S. Churchman, J. A. Spudich, and H. Flyvbjerg, *Nature Methods*, 2010, **7**, 377–381.
6. C. S. Smith, N. Joseph, B. Rieger, and K. A. Lidke, *Nature Methods*, 2010, **7**, 373–375.
7. J. W. J. Kerssemakers, E. L. Munteanu, L. Laan, T. L. Noetzel, M. E. Janson, and M. Dogterom, *Nature*, 2006, **442**, 709–712.
8. T. A. Laurence and B. A. Chromy, *Nature Methods*, 2010, **7**, 338–339.
9. L. S. Churchman, H. Flyvbjerg, and J. A. Spudich, *Biophysical Journal*, 2006, **90**, 668–671.
10. H.-X. Zhou, *J. Phys. Chem. B*, 2001, **105**, 6763–6766.
11. M. Rief, *Science*, 1997, **276**, 1109–1112.
12. B. Hamprecht and H. Kleinert, *Phys. Rev. E*, 2005, **71**, 031803.
13. D. Nettels, S. Müller-Späth, F. Küster, H. Hofmann, D. Haenni, S. Ruediger, L. Reymond, A. Hoffmann, J. Kubelka, B. Heinz, K. Gast, R. B. Best, and B. Schuler, *Proceedings of the National Academy of Sciences*, 2009, **106**, 20740–20745.